PNAS RESEARCH ARTICLE | ENGINEERING

Molecular surface programming of rectifying junctions between InAs colloidal quantum dot solids

Maral Vafaie[a,1], Amin Morteza Najarian[a,1], Jian Xu[a], Lee J. Richter[b], Ruipeng Li[c], Yangning Zhang[a], Muhammad Imran[a], Pan Xia[a], Hyeong Woo Ban[a], Larissa Levina[a], Ajay Singh[d], Jet Meitzner[d], Andras G. Pattantyus-Abraham[d], F. Pelayo García de Arquer[e], and Edward H. Sargent[a,2]

Edited by Peidong Yang, University of California Berkeley, CA; received April 1, 2023; accepted September 5, 2023

Heavy-metal-free III–V colloidal quantum dots (CQDs) show promise in optoelectronics: Recent advancements in the synthesis of large-diameter indium arsenide (InAs) CQDs provide access to short-wave infrared (IR) wavelengths for three-dimensional ranging and imaging. In early studies, however, we were unable to achieve a rectifying photodiode using CQDs and molybdenum oxide/polymer hole transport layers, as the shallow valence bandedge (5.0 eV) was misaligned with the ionization potentials of the widely used transport layers. This occurred when increasing CQD diameter to decrease the bandgap below 1.1 eV. Here, we develop a rectifying junction among InAs CQD layers, where we use molecular surface modifiers to tune the energy levels of InAs CQDs electrostatically. Previously developed bifunctional dithiol ligands, established for II-VI and IV-VI CQDs, exhibit slow reaction kinetics with III-V surfaces, causing the exchange to fail. We study carboxylate and thiolate binding groups, united with electron-donating free end groups, that shift upward the valence bandedge of InAs CQDs, producing valence band energies as shallow as 4.8 eV. Photophysical studies combined with density functional theory show that carboxylate-based passivants participate in strong bidentate bridging with both In and As on the CQD surface. The tuned CQD layer incorporated into a photodiode structure achieves improved performance with EQE (external quantum efficiency) of 35% (>1 μm) and dark current density < 400 nA cm^{-2}, a >25% increase in EQE and >90% reduced dark current density compared to the reference device. This work represents an advance over previous III-V CQD short-wavelength IR photodetectors (EQE < 5%, dark current > 10,000 nA cm^{-2}).

infrared photodetectors | heavy-metal-free colloidal quantum dots | III-V nanocrystals | molecular functionalization | energy level modification

Significance

Solution-processed III-V semiconductors hold promise for high-speed short-wave infrared (IR) photodetection, of interest for three-dimensional imaging and ranging. However, their chemical control and optoelectronic performance lag behind that of established PbS/CdS materials. We find herein that the distinct energy levels of III-V materials create an energy misalignment relative to known hole transport materials. We develop molecular surface modifiers tailored for energy level tuning of indium arsenide (InAs) colloidal quantum dots (CQDs), thus providing InAs size-tuned hole transport materials. The rectifying junction among InAs CQD layers yields significantly improved performance compared to previously reported III-V short-wave IR CQD photodetectors. This study reports a rectifying junction between III-V CQD solids and provides design principles for generation of liquid-processed IR optoelectronic materials.

In solution-processed optoelectronics, heavy metal-free III-V CQDs (colloidal quantum dots) hold promise in light of their higher thermal stability and their lower dielectric constant compared to II-VI and IV-VI chalcogenide CQDs (1–3). Among these desirable properties, each traceable to the semiconductors' more covalent character, the lower dielectric constant is relevant to increasing speed, pertinent to machine vision, augmented reality, and autonomous vehicles. In terms of spectral range, it is particularly relevant to explore performance in the short-wavelength infrared (SWIR)—ranging from 1,000 to 2,500 nm—in view of its high maximum permissible exposure for lasers in this spectral region (4).

Recent advances in diffusion-dynamics-controlled synthesis (1, 5) of III-V materials have enabled the synthesis of large-diameter (4-nm to 8-nm) InAs CQDs featuring an absorption edge beyond the 1.1-μm detection limit of silicon, and the community has recently made strides in achieving promising size uniformity even at these higher average dot radii (Fig. 1 *A* and *B* and *SI Appendix*, Figs. S1–S3). When growing CQDs, modifications occur in their conduction or valence bandedges (6). Conventional transport layers, such as polymers and metal oxides, offer limited variation in energy levels that can match the requirements for SWIR QDs. Previous investigations of IV-VI CQDs demonstrated a substantial downward shift in the conduction band minimum (CBM) as the bandgap was tuned from 900 nm to 1,100 nm (7). In contrast, for InAs CQDs, the 0.2-eV reduction in the bandgap shifts the valence band maximum (VBM) from 5.27 eV to 5.07 eV (Fig. 1*C* and *SI Appendix*, Fig. S4 and *Text Note. 2*).

Molybdenum oxide (MoOx) works well as an efficient hole-selective recombination layer in silicon, organic, perovskite, and PbS CQD-based (8–11) diodes and was recently used successfully in near-IR InAs CQD photodiodes (940-nm peak response) (2). However, when—in preliminary studies of SWIR InAs CQD devices—we employed MoOx, we observed poor rectifying behavior and high dark current (Fig. 1*D*). A survey of widely used polymer hole transport materials (HTL) (7) led to improved rectification but a severe loss in external quantum efficiency (EQE) (Fig. 1 *E* and *F* and *SI Appendix*, Fig. S5).

Author contributions: M.V., A.M.N., and E.H.S. designed research; M.V. performed research; L.J.R., R.L., M.I., P.X., H.W.B., and L.L. contributed new reagents/analytic tools; M.V., J.X., A.S., J.M., and A.G.P.-A. analyzed data; J.X. theoretical calculations; and M.V., A.M.N., Y.Z., F.P.G.d.A., and E.H.S. wrote the paper.

The authors declare no competing interest.

This article is a PNAS Direct Submission.

[1]M.V. and A.M.N. contributed equally to this work.

[2]To whom correspondence may be addressed. Email: ted.sargent@utoronto.ca.

This article contains supporting information online at https://www.pnas.org/lookup/suppl/doi:10.1073/pnas.2305327120/-/DCSupplemental.

Published October 3, 2023.

Fig. 1*C* shows the estimated band alignments and suggests an explanation of this finding: Holes generated in the InAs CQD active layer diffuse toward the HTL and encounter a barrier caused by the HTL deeper VBM, hindering their extraction. On the other hand, the nonoptimal band alignment at this interface results in a higher density of electrons on the HTL side, leading to increased surface recombination. Similarly, in the case of MoOx, its role as an efficient hole extractor relies on achieving a proper band alignment between the MoOx CBM and the semiconductor VBM. Without this alignment, there is a higher probability of photogenerated holes recombining with electrons from the active layer, resulting in a loss of open-circuit voltage, reduced photocurrent, and elevated dark current (Detailed explanation of the MoOx function in our photodiode structure is presented in *SI Appendix, Text Note. 3*).

These initial findings prompted us to ask the following: Could we develop a rectifying junction between two InAs CQD active layers, something that would rely on doping and energy alignment control in distinct CQD solids, thereby enhancing charge transport/blocking at this interface (Fig. 1*G*) (12)?

Results and Discussion

First, we evaluated the possibility of elemental doping: However, recent studies of this approach in InAs CQDs have shown the presence of significant densities of in-gap states (13, 14): For example, doping with zinc has been accompanied by broadening and red shifting of the absorption edge, a finding attributed to lattice distortion (15). Alternatively, we shifted our focus to electrostatic tuning of energy levels using surface ligands, an approach previously implemented successfully in IV-VI CQDs (13, 16). In these studies, the introduction of short dithiols such as 1,2-ethanedithiol (EDT) resulted in an upward shift of the bandedges in PbS CQD solids, allowing for the development of QD-based hole transport layers (QHTLs) (9).

In our attempts to apply a similar process chemistry using InAs, we found that ostensibly slow kinetics of EDT with III-Vs led to failure to achieve a complete solid-state ligand exchange (*SI Appendix*, Fig. S8). The result was a limited bandedge shift: The valence bandedge remained well deeper than 5 eV even after attempted two-step surface modification (17).

These considerations led us to posit a set of design principles for selecting ligands to passivate CQD surfaces with tunable energy levels. First, ligands incorporate an energy level–modifying group (EMG) having an electron-donating nature, with the goal of upshifting the CQD energy levels (18). Second, they include an anchoring functional group (AG) to attach the organic module to the CQD surface. Third, they should have a short organic backbone to minimize the interdot spacing and provide charge transport within CQD solids (19). We explored the application of these guidelines to ligand candidates tailored for InAs CQDs.

Focusing on thiolate and carboxylate AGs, known as linkers for III-V material (20, 21), we evaluated a number of ligand classes. Surface modification of InAs CQDs with an aromatic ligand, such as benzoic acid, shifted energy levels upward, but the bulky nature of the molecule hindered charge transport (*SI Appendix*, Fig. S9). Altering the CQD surface with molecules lacking carbon in their backbone, including acetic acid, resulted in incomplete exchanges (22). Therefore, we restricted our search to ligands with a 1- to 2-carbon chain length. Bifunctional ligands, such as EDT, caused CQD aggregation in the solution. The treatment of InAs CQDs with ligands of nitrogen-centered EMGs, such as dimethylglycine, resulted in limited solubility, potentially caused by interaction

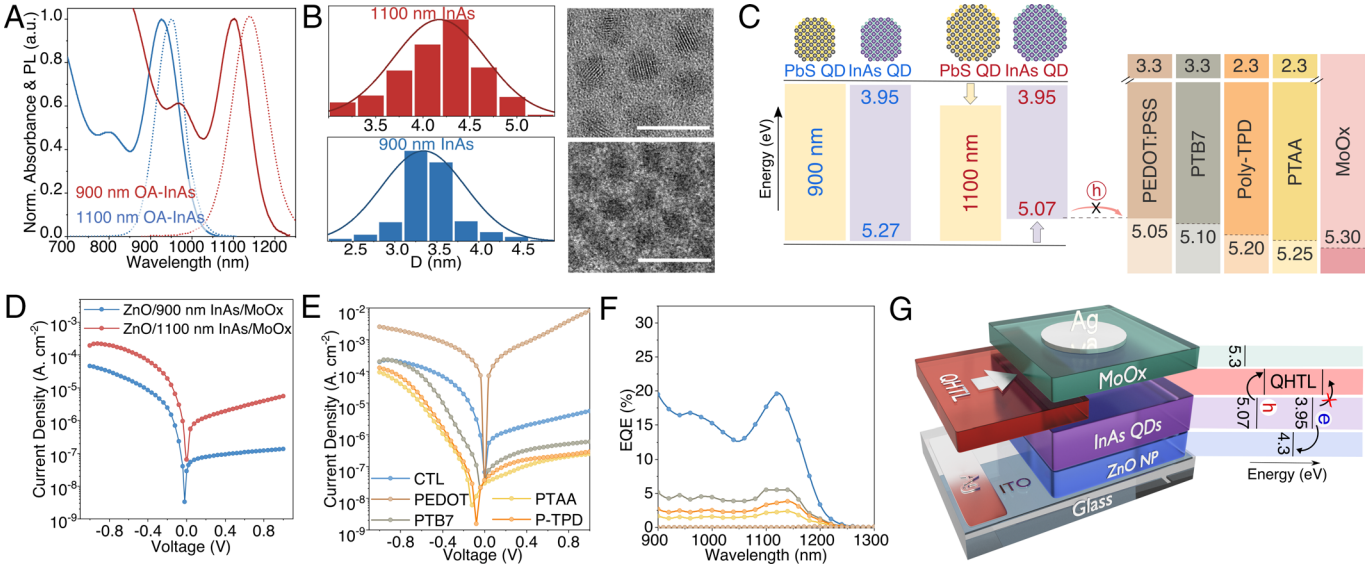

Fig. 1. Energy level alignment for SWIR-bandgap InAs diodes. (*A*) Absorbance and photoluminescence spectra of as-synthesized InAs CQDs with peak sensitivity in the range of 900 nm (<1.37 eV) and 1,100 nm (<1.12 eV). The photophysical parameters are reported in *SI Appendix*, Fig. S1. (*B*) High-resolution transmission electron microscopy (HR-TEM) of 900-nm and 1,100-nm InAs CQDs (Scale bar, 10 nm), with histograms of size distribution. The average diameter and standard deviation values have been calculated to be 3.42 ± 0.44 nm for the 900 nm QDs and 4.34 ± 0.47 nm for the 1,100-nm InAs CQDs (sample size >500). More information is provided in *SI Appendix, Text Note. 1* and Figs. S2 and S3. (*C*) Relative bandedge positions in InAs CQDs after increased particle size in contrast with observations in the PbS CQD system. UPS and absorption spectra of InAs CQDs are provided in *SI Appendix*, Fig. S4. (*D*) Effect of nonoptimal band alignment of 1,100-nm InAs CQDs on the photodiode behavior compared with 900-nm InAs CQDs in ZnO/CQD/MoOx configuration. The current density-voltage plot is measured in a dark condition. (*E*) Dark current density-voltage (J-V) characteristics, and (*F*) EQE (at 0 V) of InAs photodiodes with incorporated polymer HTLs in comparison to the control device with MoOx HTL (CTL). *SI Appendix*, Fig. S5 provides the same performance metrics for polymer HTLs of lower thickness. (*G*) Schematic of the proposed photodiode architecture with the incorporation of a quantum-tuned hole transport layer with suitable energy levels. The favorable band alignment of this HTL is projected to lead to improved hole extraction and electron blocking. The proposed band diagram is based on the reported energy levels for MoOx (shown as green), ZnO (shown as blue) (8), measured values for the 1,100-nm InAs photoactive layer (shown as purple) and a QHTL with ideal CBM and VBM levels (shown as red). The role of MoOx in this modified structure is explained in *SI Appendix, Text Note. 3*.

between the head group and the CQD surface. This led us to two candidate ligands (Fig. 2*A*): 2-mercaptoethanol (MCE) with hydroxyl (OH) and methoxyacetic acid (MTA) with methoxy (O-CH3) functional groups.

In addition to matching the valence bandedge to facilitate hole extraction, it is crucial for the HTL to create a sufficient energetic barrier for electron transfer. The size-induced modulation of the CQD bandgap offers an additional means of bandedge tuning independently of electrostatic effects. In our design of QHTL for the SWIR active layer, we specifically focused on QHTL with a bandgap of 900 nm. This choice would enable us to maximize the potential of CQDs' two-level tuning capability by significantly raising the CBM edge and the electron blockage ability of the QHTL.

We began by conducting a solution-phase exchange to replace native oleic acid ligands on the surface of 900-nm InAs CQDs with the molecules of interest. Comparing IR spectra (Fig. 2*B*) of the pristine ligands with the CQD films after ligand exchange, we see the disappearance of S-H stretches at 2,550 cm^{-1} in the case of MCE-InAs; and of saturated C=O stretch at 1,720 cm^{-1} and O-H stretch at ≈ 3,000 cm^{-1} for MTA-InAs, suggesting that the linkers are affixed to the quantum dot surface by the anchoring groups. X-ray photoelectron spectroscopy (XPS) (Fig. 2 *C* and *D* and *SI Appendix*, Table S2) shows the appearance of a C-O-C shoulder peak at 286 eV and the rise of the O=C-O bond with respect to the C-C main peak, indicating MTA on the InAs CQD surface. Following the MCE exchange, overlapping spin–orbit split states were detected in the S 2p region at 162 eV, consistent with chemically bonded thiols (20).

OA-capped InAs CQDs show an arsenic-to-indium ratio of ≈ 0.7, whereas, following exchange, this approaches unity (Fig. 2*E*). This observation is consistent with previous reports (22) where the as-synthesized QDs exhibit an indium-rich surface, attributed to an indium-oleate ligand shell, that is removed upon an effective ligand exchange. The absorption spectra measurement before and after ligand exchange (*SI Appendix*, Fig. S10) confirms that this observed surface reconstruction does not originate from dot etching. There is a slight redshift after the exchange with MCE and MTA, a finding previously observed in several CQD and ligand systems. This ligand-induced redshift has been ascribed to carrier wavefunction delocalization owing to ligand functionalization and to the difference in the dielectric permittivity of the nonpolar and polar environment (23–28). From ultraviolet photoemission spectra (UPS) measurements (Fig. 2*F* and *SI Appendix*, Fig. S11), we see an upward energy level shift upon CQD surface functionalization: The shallow VBMs obtained for MCE-InAs (4.95 eV) and MTA-InAs (4.88 eV) suggest promise in hole extraction/electron blocking.

We investigated the photophysical properties of the MTA- and MCE-functionalized CQDs with the aid of absorption, steady-state photoluminescence (PL), and time-resolved PL. At a given concentration of CQD solution, MCE capped dots showed lower PL intensity compared to MTA (Fig. 3*A*). The MTA-InAs ink exhibits a twofold longer average carrier lifetime (≈ 3.4 ns) than does the MCE-InAs ink (≈ 1.6 ns). MCE-InAs have a lower PL quantum efficiency and a shorter carrier lifetime, suggesting more quenching-related traps (Fig. 3*B* and *SI Appendix*, Table S3) (29). The conductivity of InAs CQD thin films was examined using an interdigitated electrode (IDE) structure (Fig. 3*C*). Enhanced passivation of surface trap states using MTA molecules resulted in four times higher conductivity for the MTA-InAs film compared to the MCE-InAs film.

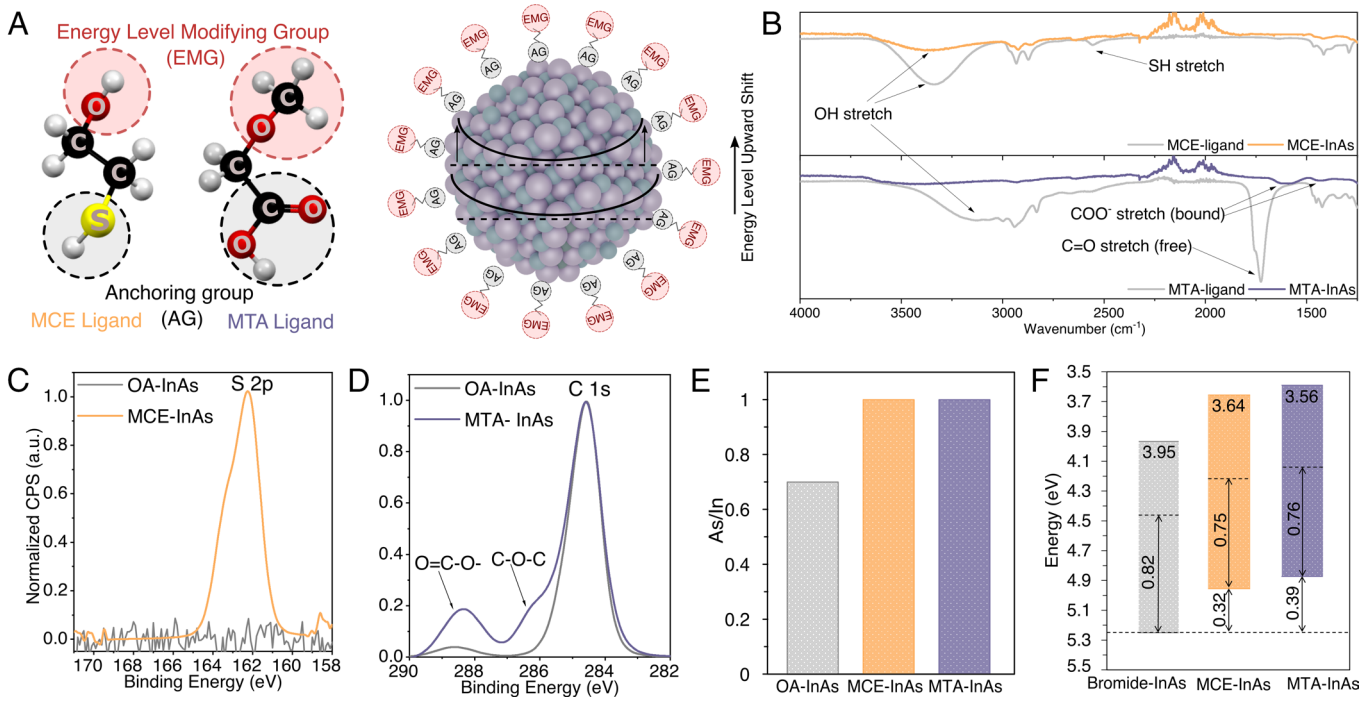

Fig. 2. Donor molecular surface modifiers enabling energy level modification in InAs CQDs. (*A*) The structure of the two employed organic ligands MCE and MTA and their application in electrostatic energy level modification of InAs CQDs. Both ligands contain an AG that links to the CQD surface after ligand exchange and enables the functionalization of the ligand's EMG. The electron-donating nature of the EMGs is expected to shift the CQD energy levels upward. (*B*) IR spectra of the InAs CQD films after ligand exchange with MCE (MCE-InAs) and MTA (MTA-InAs) molecules. For each panel, the gray line shows the spectra of the pure organic molecule. (*C*) High-resolution XPS spectra of S 2p, and (*D*) of C 1s for InAs CQD films before (OA-InAs) and after the exchange with MCE and MTA molecules. (*E*) Calculated In/As ratio for InAs CQD films before and after the exchange with MCE and MTA molecules. Further information on the XPS spectra of these samples is provided in *SI Appendix*, Table S2. (*F*) Energy band diagram of 900-nm InAs CQD films processed with indium bromide-based, MCE, and MTA ligand exchange. The calculated VBM values of these exchanged films are 5.27 eV, 4.95 eV, and 4.88 eV, respectively. The original UPS are provided in *SI Appendix*, Fig. S11.

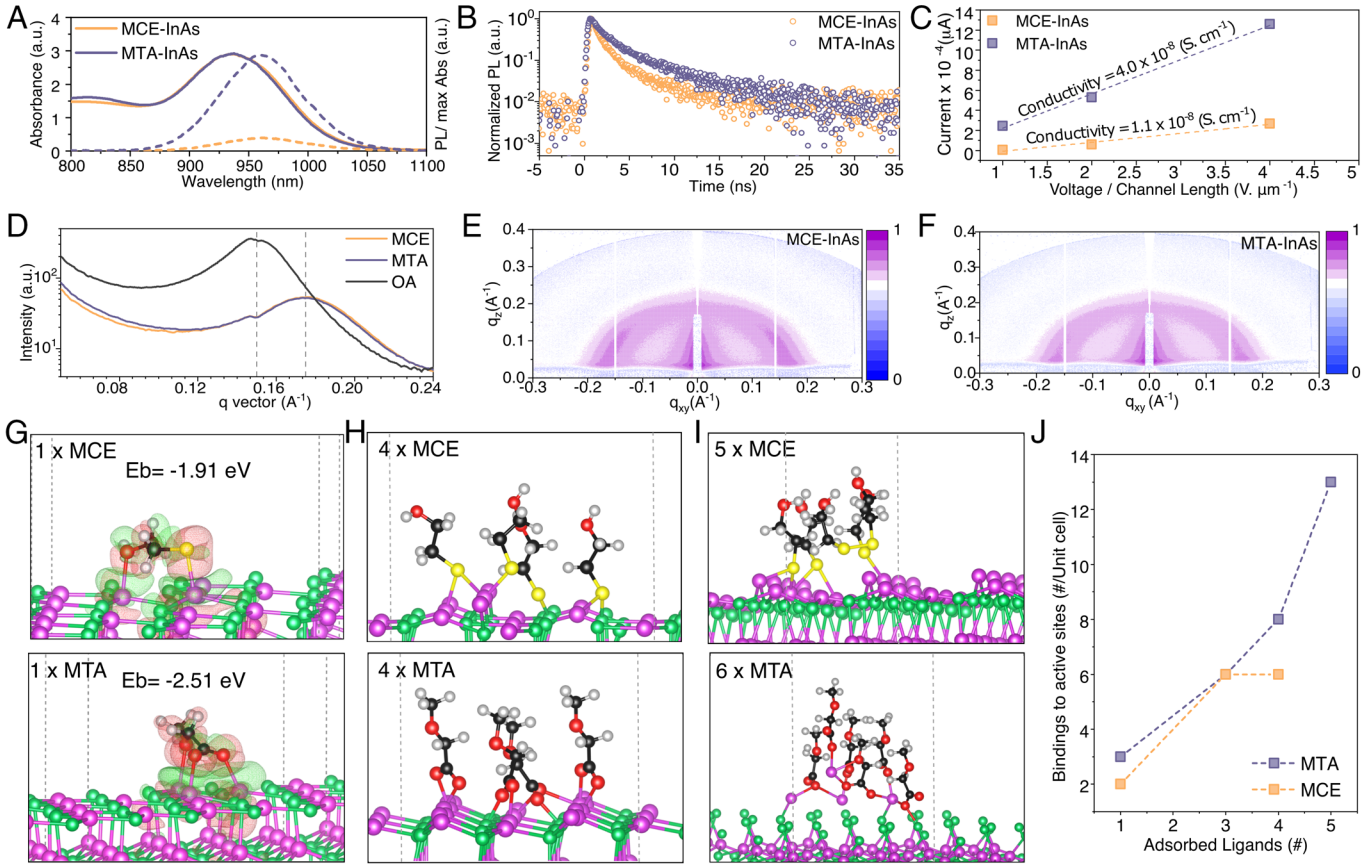

Fig. 3. Molecular surface modifiers and surface passivation scheme. (*A*) Absorbance and PL spectra of MCE- and MTA-InAs CQDs solutions. The spectra for the as-synthesized InAs CQD solution are presented in *SI Appendix*, Fig. S10. (*B*) Comparison of time-resolved PL spectra of MCE- and MTA-InAs CQDs solutions. Extracted data are reported in *SI Appendix*, Table S3. The spectrum of the as-synthesized material is compared in *SI Appendix*, Fig. S12. (*C*) Comparison of the conductivity of MCE- and MTA-InAs films deposited on the IDE structures based on measurement of current at 10 V voltage for different channel lengths (2.5 to 10) μm. Details of measurement and calculations are discussed in the Methods section. (*D*) Azimuthal integration of GISAXS 2D patterns of OA-, MCE-, and MTA-InAs CQD films shown in e-f and *SI Appendix*, Fig. S13. The interdot spacing is obtained by determining the maximum in I(q) obtained by fitting it to an exponentially modified Gaussian. (*E*) GISAXS 2D patterns of MCE- and (*F*) MTA-InAs CQD films on Silicon substrate. (*G*) Calculated binding energy and differential charge density of a single MCE and MTA molecules at their most stable position on the (111) surface of one (2×2) InAs unit cell (indium and arsenic atoms are respectively defined by magenta and green colors). An isolated molecule of MCE or MTA stabilizes on the surface by linking its deprotonated anchoring group or oxygen lone pair electrons of functional groups to indium active sites. (*H* and *I*) Molecule–InAs surface interaction when a greater number of ligands are introduced and optimized by DFT. With the addition of more ligands to the system, MCE and MTA molecules become more upright in binding configurations. The incorporation of excessive ligands into the system (5 for MCE and 6 for MTA molecule) results in surface instability and detachment of ligands/surface indium atoms. (*J*) The number of binding sites between the adsorbed molecule (MCE or MTA) and the surface active sites (In or As). The number of ligands per unit cell area is increased as discussed in DFT calculations and shown in *G*–*I*.

From grazing-incidence small-angle X-ray scattering (GISAXS) (Fig. 3*D*), the interdot spacing for functionalized CQD films is ≈ 4.3 nm (decreased from ≈ 5 nm in OA-InAs films). In addition, when comparing the GISAXS and grazing-incidence wide-angle X-ray scattering (GIWAXS) patterns of InAs CQD–exchanged films (Fig. 3 *E* and *F* and *SI Appendix*, Figs. S13 and S14), both MTA-InAs and MCE-InAs exhibit a low level of ordering in dot packing and isotropic crystallographic plane orientation. The variation in photophysical properties of functionalized dots is primarily a function of the surface passivation efficiency, rather than of the morphology and ordering of the dots in the film.

Density functional theory (DFT) studies that model ligand-quantum dot interactions suggest possible explanations for the distinct passivating behavior of each ligand (Fig. 3 *G*–*I*). We began by first considering a single molecule configuration with the lowest (most favorable) energy on one unit cell of the (2×2) InAs surface. For the purpose of comparison, we specifically selected the (111) facet as a representative among the exposed crystal facets of InAs, enabling access to both In and As terminations (*SI Appendix*, Fig. S15). The MCE ligand's thiolate anchors to one active site on the InAs surface, while MTA's carboxylate binds to two active centers in a bidentate format. This is consistent with previous research showing that carboxylate ligands primarily interact with multiple active surface centers through bridging bidentate coordination (30, 31). Calculation of binding energy values indicates that the MTA ligand attaches more strongly to the InAs CQD (111) surface (–2.51 eV) than does the MCE ligand (–1.91 eV). Carboxylate linkers may be able to passivate more sites per molecule and be less prone to detach from the CQD surface than MCE. Further electronic structure analysis is needed in exploring the formation of mid-gap trap states on different surfaces for each ligand scenario.

Computationally, we then sought to increase progressively the number of ligands per area of the InAs unit cell. The ligands passivate additional exposed indium and arsenic sites as the ligand density is titrated up, until reaching a threshold beyond which unstable ligands detach from the InAs bulk (Fig. 3 *G*–*I*). Limited ligand availability per surface area emphasizes the importance of the ligand's anchoring capacity for efficient surface passivation. For the simulated unit cells with maximum ligand coverage, MTA ligands show a higher number of bindings to surface active sites compared to MCE ligands (Fig. 3*J*), in agreement with the ability

of carboxylate anchors to form multiple coordination. This suggests that MTA may offer a better passivation strategy.

The control photodiodes with MoOx as the hole transport layer (labeled CTL) exhibited a dark current of 7,000 nA cm^{-2} (at 1 V bias) while achieving a 20% EQE. When we incorporate the QHTLs into photodiodes, we see improved dark current and photocurrent (Fig. 4 *A* and *B*). Once we optimized thickness, we obtained a two-order-of-magnitude improvement in dark current, reaching 400 nA cm^{-2} at 1 V reverse bias. The open-circuit voltage (V_{oc}) increases from 40 mV (controls) to 120 mV for the MCE QHTL and to 200 mV in MTA QHTL devices. The EQE reached 31% at the 1,120-nm excitonic peak for MTA devices. This corresponded to an increase in the internal quantum efficiency (IQE) from 70 (controls) to 90% for devices using MTA QHTLs. We link this to lower photocarrier loss at the interface between the absorber and the MoO_x. MTA devices achieved a peak responsivity of 0.3 A/W at 1,120-nm excitation under a 1-V operating bias (Fig. 4*C*). The CTL devices show performance higher than those reported in prior III-V CQD SWIR photodetectors—these prior works had EQE < 5% and dark current > 10,000 nA cm^{-2}. We note here that CQD synthesis, passivation scheme, photodiode architecture (p-i-n vs. n-i-p), and the selection of electron and hole transport layers have all benefited from progress since the time of publication of ref. 32.

We explored the trend in dark current and quantum efficiency of devices with increasing QHTL thickness (Fig. 4 *D* and *E* and *SI Appendix*, Table S4). The EQE is maximized for a 15-nm-thick QHTL in the MTA case and at a 10-nm thickness for the MCE case. We suggest that a lower extent of passivation and/or conductivity in MCE may account for this. The benefits to dark current density with increased QHTL thickness also plateau near these optimized thicknesses: The benefits obtained from the presence of the QHTL have been accrued by these thicknesses, and further increase provides no further returns.

The speed of response of the photodetectors was assessed, and the fall times (from 90 to 10% of normalized photocurrent) were determined to be 1.5 μs for all examined photodiodes (Fig. 4*F*). In solution-processed materials, including CQDs and perovskites, the main factor limiting the detector response time is the geometrical capacitance, depending on parameters such as the dielectric constant, area, and thickness of the active material (33). In the case of InAs CQDs, measurements indicate a lower permittivity compared to PbS CQDs (2). We compared the temporal response of our InAs CQD photodetector, with the same pixel area, to that of a SWIR PbS CQD photodetector (*SI Appendix*, Fig. S16). The results indicate that InAs CQD photodiodes exhibit a faster temporal response than their PbS counterparts in the capacitance-limited regime. Further investigation is required to explore the boundary between the capacitance-limited time response and the transport-limited regime (mobility-dependent) for InAs CQD photodetectors.

Photocurrent stability of an unencapsulated and encapsulated MTA-based photodetector was measured at 0 V applied bias under the exposure of a filtered white light source in ambient air (*SI Appendix*, Fig. S17). The encapsulated device demonstrated retention of 88% of the initial photoresponse after 3 h of operation. In contrast, the unencapsulated device photocurrent dropped below 50% under the potential effects of air exposure and oxidation. The stability of the QHTL ink under air exposure is also studied and presented in *SI Appendix*, Fig. S18.

In summary, this work reports the development of InAs size-tuned hole transport materials based on molecular donor functionalization, leading to a rectifying junction between III-V CQD solids. SWIR InAs CQD photodiodes achieve as a result 35% EQE and 400 nA cm^{-2} dark current density, representing 25% and 90% improvement in EQE and dark current compared to the control device. These results outperform prior III-V CQD SWIR photodetectors with a 7× increase and a 25× decrease in EQE and dark current, respectively. The approach of surface

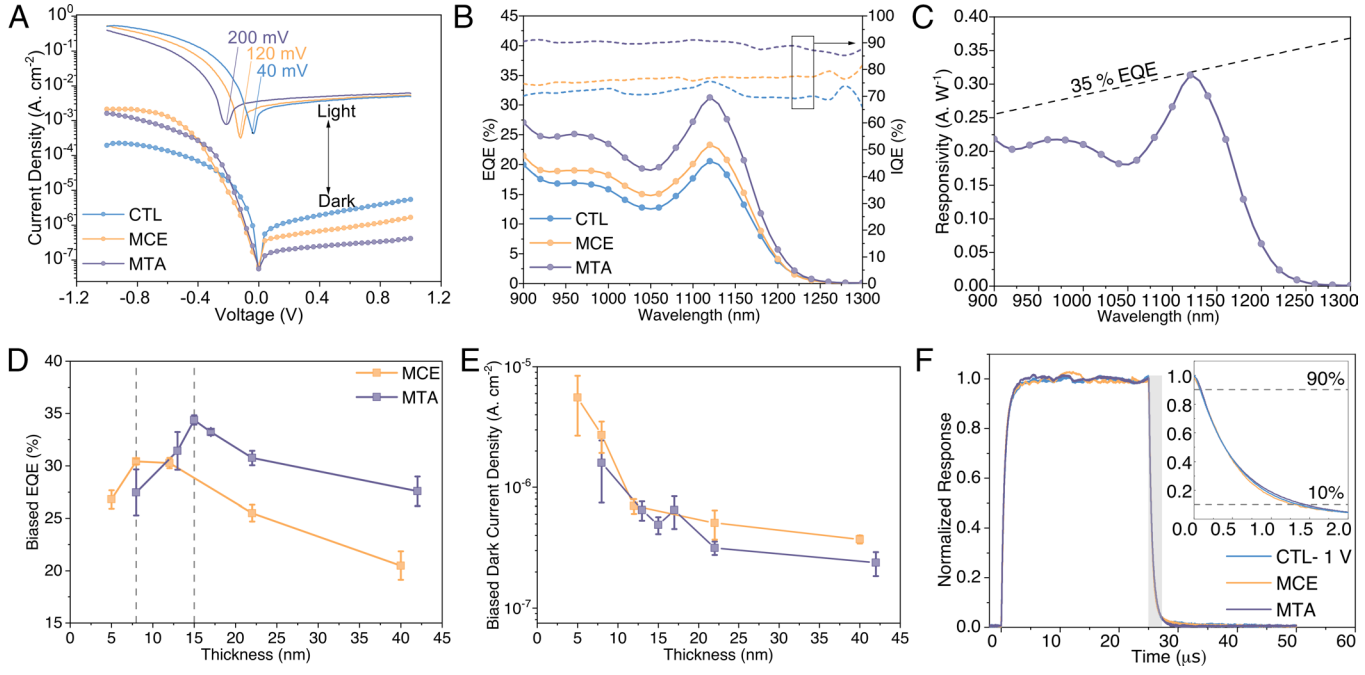

Fig. 4. Effect of QHTLs on the performance of the fabricated SWIR InAs photodetector. (*A*) Enhanced dark and illuminated J-V characteristics of fabricated InAs photodiodes using MCE- and MTA-based QHTLs in comparison to the reference device without QHTL (CTL). For illumination, a 940-nm fiber-coupled laser source with 2-mW output power with an illumination area of 0.049 cm^2 was used. (*B*) EQE (at 0 V applied bias) and estimated IQE of the devices presented in *A*. (*C*) Responsivity (at 1 V) of the InAs CQD detector using MTA-based QHTL. (*D*) Trend in biased EQE (at 1 V, at 1,120-nm wavelength) and (*E*) dark current (at 1 V applied bias) with a thickness of MCE- and MTA-based QHTLs for fabricated photodetectors. The average and standard deviation values are listed in *SI Appendix*, Table S4. (*F*) Measured transient photocurrent for QHTL-based and CTL photodetectors at 1 V applied bias for pixels with 0.049-cm^2 active area. The inset shows the decay behavior of the temporal response for each photodetector.

modification of InAs CQDs with carboxylate and thiolate linkers, coupled with functionalized organic donors, enables tuning of the bandedge of the CQD solid. It appears that carboxylate-based linkers interact strongly with both anionic and cationic InAs active surface sites, enabling the passivation scheme.

Materials and Methods

Materials. Indium acetate [$In(OAc)_3$, 99.99%], oleic acid (OA, technical grade, 90%), dioctylamine (DOA, Aldrich, ≥97%), 1-octadecene (ODE, 90%), N, N-dimethylformamide (DMF, 99.8% anhydrous), octane (99% anhydrous), 1-butanol (BuOH, 99.8% anhydrous), toluene (Tol, 99.8% anhydrous), ammonium acetate (AA, 99.999%), 2-MCE (99%), MTA (98%) were purchased from Sigma-Aldrich. Tris(trimethylsilyl)arsine [$(TMSi)_3As$] was purchased from Dockweiler Chemicals Inc. Indium (III) bromide ($InBr_3$, 99.999% anhydrous) was purchased from Strem Chemicals, Inc. All the mentioned chemicals were used as received.

InAs CQD Synthesis. InAs seed and cluster solutions were prepared using indium acetate $In(OAc)_3$ and Tris(trimethylsilyl) arsine $(TMSi)_3As$ precursors. For the seed solution, 1 mmol $In(OAc)_3$ and 3 mmol OA were degassed in 5 mL of ODE at 110 °C under a vacuum (~0.5 mbar) overnight. In a nitrogen-filled glove box, 0.5 mmol $(TMSi)_3As$ was mixed with 1.5 mmol DOA and 1 mL ODE and reacted for 10 min at 60 °C. The degassed indium precursor solution was heated to 300 °C under nitrogen conditions, and the As precursor solution was rapidly injected. For the cluster precursor, 2.5 mmol $In(OAc)_3$ and 7.4 mmol OA were degassed in 12.6 mL of ODE at 110 °C overnight. For the As precursor solution, 1.25 mmol $(TMSi)_3As$ was mixed with 3.7 mmol DOA and 2.5 mL ODE, and reacted for 10 min at 60 °C in the glovebox. Then, In and As precursor solutions were reacted at 40 °C under nitrogen conditions for 15 min. The InAs nanoclusters solution was immediately loaded into a 20-mL syringe and continuously injected into the InAs QD seed solution via a syringe pump at an average injection rate of 2 mL/h at a growth temperature of 290 °C for 3 to 12 h. The nanocluster solution was stable during the injection. The absorption spectra of the crude solution were monitored throughout the growth stage to obtain the desired peak absorbance (bandgap). Once the desired dot size was achieved, the flask was cooled down to 115 °C using an air gun and then further cooled from 115 °C to 35 °C using an ice bath. The synthesized InAs QD crude solution was purified three times with butanol (as the antisolvent for QD precipitation) and hexane (as the solvent for QD redispersion) before usage.

Device Fabrication. Indium tin oxide (ITO) glass substrates (Delta Technologies, 80 to 90 ohm square^{-1}) were cleaned and used as conductive substrates. For the electron transport layer, a ZnO nanoparticle solution was prepared and spin-coated on the ITO under ambient conditions resulting in an ≈120-nm-thick layer (9). The rest of the fabrication procedures were carried out in a N_2-filled glovebox. For the active layer, the as-synthesized 1,100-nm OA-InAs CQDs were processed by a liquid-phase solution exchange as previously reported (2). In brief, a mixture of $InBr_3$/AA solution was prepared with $InBr_3$ (0.1 mol L^{-1}, 0.18 g) and ammonium acetate (0.04 mol L^{-1}, 0.023 g) in 5 mL of DMF. About 5 mL of CQD octane solution (10 mg mL^{-1}) was added to 5 mL of the precursor solution. These were vortexed for (1 to 2) min until the CQDs were completely transferred to the DMF phase, followed by washing three times with octane. After ligand exchange, CQDs were precipitated via the addition of toluene (≈ 10 mL) and separated by centrifugation. After 10 min of vacuum drying, the CQDs were then redispersed in DMF (200 mg mL^{-1}) and were spin-coated at (2,000 to 3,000) rpm (1 rpm = 2π/60 rad/s) resulting in an ≈120-nm-thick layer. The films were then annealed at 75 °C for 20 min. The QHTL inks were prepared using the as-synthesized 900-nm OA-InAs CQDs with liquid-phase solution exchange. Exchange solutions were prepared by adding 200 μL of the MCE or MTA to 5 mL of DMF. About 10 mL of CQD octane solution (10 mg mL^{-1}) was added to the precursor solution. These were vortexed for (1 to 2) min until the CQDs were completely transferred to the DMF phase, followed by washing three times with octane. After ligand exchange, CQDs were precipitated via the addition of toluene and separated by centrifugation. After 10 min of vacuum drying, the CQDs were then redispersed in DMF and spin-coated at 1,000 rpm. The final concentration of the QHTL inks depends on the required thickness and was changed in the range of (5 to 100) mg mL^{-1} to optimize the thickness for each ligand. As a final step, MoO_3 (14 nm) and Ag (140 nm) were deposited by using thermal evaporation.

Characterizations. Absorption and steady-state PL of the solutions were measured in a homemade setup consisting of Maya2000 Pro (Ocean Optics) and NIRQUEST (Ocean Optics) spectrometers. A stabilized tungsten-halogen light source (SLS201L–Thorlabs Inc.) and a 365-nm UV LED were used as illumination sources. Solutions were kept in a tightly sealed quartz cuvette with a 1-mm path length and were placed in a SQUARE ONE cuvette holder (Ocean Optics). The optical absorption measurements of the thin films were performed with a Perkin-Elmer Lambda 950 UV–vis–NIR spectrophotometer. Time-resolved PL was measured using a Horiba Fluorolog time-correlated single-photon-counting system with photomultiplier tube detectors. High-resolution transmission electron microscopy measurement of the samples was carried out on a Hitachi H3300F. IR spectra were obtained in the attenuated total reflectance mode using a Fourier-transform IR spectrometer (Thermo Scientific iS50) in the spectral range of 4,600 to 1,200 cm^{-1}. Samples were prepared on glass substrates. To measure UPS, CQD films on ITO glass were measured in an ESCALAB 250Xi system using a helium discharge lamp (He Iα, energy = 21.22 eV) as the ultraviolet source. XPS spectra of the spin-coated films were measured in N_2 with a Thermo Scientific K-Alpha System with an Al Kα source. For conductivity measurements, CQD thin films were spin-coated on a prepatterned interdigitated silver electrode with channel lengths varying in the range of 2.5 to 100 μm. The channel width and thickness were respectively 4 mm and 20 nm. The samples were scanned in the range of −10 V to 10 V, while the samples were illuminated with a 365-nm UV LED. The output current was measured using a Keithley 2400 source meter. Both GIWAXS and GISAXS were performed at 13.5 keV at the complex materials scattering beamline, 11-BM, at NSLS-II. Sample-to-detector distance and beam center were determined from a silver behenate standard. GIWAXS data were recorded in a vacuum at an angle of incidence of 0.15°, while GISAXS was recorded at 0.20°. GIWAXS was recorded with a Pilatus 800K detector at a nominal distance of 257 mm, and GISAXS with a Pilatus 2M detector at a nominal distance of 1,993 mm. Data were analyzed in the Nika software package (34). Detector images were tiled in the vertical direction to remove horizontal detector artifacts. Pole figures are symmetrized about $\chi = 0$ to remove vertical detector artifacts.

Dark current–voltage (I-V) measurements were taken using a Keithley 2400 source meter without any illumination for devices with 0.1-cm^2 pixel areas. For current–voltage measurement under illumination, a 940-nm fiber-coupled laser source with 2-mW output power with an illumination area of 0.049 cm^2 was used. I–V curves were scanned from −1 V to +1 V at 0.04-V interval steps without delay time between voltage steps. The EQE of the photodiodes was measured using a QUANTX-300 Newport measurement system at 0 V and −1 V external bias. IQE spectra were then estimated using the EQE (0 V)/EQE (1 V) formula (35). Measurements were taken under constant nitrogen flow. The operational stability of unencapsulated and encapsulated photodetectors was evaluated by monitoring the photocurrent at 0 V under the exposure of a filtered white light source with a power intensity of 0.02 sun (simulated AM 1.5G illumination–Sciencetech) in ambient air for a duration of 3 h. The devices were encapsulated using UV epoxy resin in the N_2 glovebox environment. Temporal response of the photodetectors was recorded for devices with an active pixel area of 0.049 cm^2 using an 8-GHz oscilloscope (Tektronix, MSO64B). An 850-nm vertical-cavity surface-emitting laser (T85V-P-LCLC0) modulated at a frequency of 2 kHz using an arbitrary function generator (Tektronix, AFG31000 Series) was used to illuminate the pixels. The photodetector signal was preamplified (10^3 V/A) using a preamplifier (Femto DHPCA-100). The photodetector was biased through the preamplifier when applicable.

Theoretical Calculations. First-principles calculations based on DFT were carried out using Vienna Ab initio Simulation Package (36). We used the generalized gradient approximation of the Perdew–Burke–Ernzerhof functional as the exchange-correlation functional (37). We included the DFT-D3 method for the van der Waals correction (38). The plane-wave cutoff energy of 400 eV was used. The energy and force convergence criteria were set to 10 to 5 eV and 0.02 eV Å to 1, respectively. We adopted the experimentally observed In-vacancy (2×2) reconstruction structure of the InAs (111) surface model in simulation (39). Different adsorption sites of ligands on InAs surfaces were considered.

Disclaimer. Certain commercial equipment, instruments, or materials are identified in this paper to foster understanding. Such identification does not imply

recommendation or endorsement by the National Institute of Standards and Technology, nor does it imply that the materials or equipment identified are necessarily the best available for the purpose.

Data, Materials, and Software Availability. All study data are included in the article and/or *SI Appendix*.

ACKNOWLEDGMENTS. This research used beamline 11BM (CMS) of the National Synchrotron Light Source a US Department of Energy (DOE) Office of Science User Facility operated for the DOE Office of Science by Brookhaven National Laboratory under contract No. DE-SC0012704. We gratefully acknowledge funding from STMicroelectronics.

Author affiliations: [a]The Edward S. Rogers Department of Electrical and Computer Engineering, University of Toronto, Toronto, ON M5S 3G4, Canada; [b]Materials Science and Engineering Division, National Institute of Standards and Technology, Gaithersburg, MD 20899; [c]National Synchrotron Light Source II, Brookhaven National Laboratory, New York, NY 11973; [d]STMicroelectronics, Digital Front-end Manufacturing and Technology, Technology for Optical Sensors, Fremont, CA 94538; and [e]Institut de Ciències Fotòniques, The Barcelona Institute of Science and Technology, Barcelona 08860, Spain

1. Y. Kim *et al.*, III–V colloidal nanocrystals: Control of covalent surfaces. *Chem. Sci.* **11**, 913–922 (2019).
2. B. Sun *et al.*, Fast near-infrared photodetection using III–V colloidal quantum dots. *Adv. Mater.* **34**, 2203039 (2022).
3. H. Zhao, M. Chaker, N. Wu, D. Ma, Towards controlled synthesis and better understanding of highly luminescent PbS/CdS core/shell quantum dots. *J. Mater. Chem.* **21**, 8898–8904 (2011).
4. A. L. Augustoni, Laser selection based on maximum permissible exposure limits for visible and middle-near infrared repetitively pulsed lasers (No. SAND2004-1111, Sandia National Laboratories (SNL), Albuquerque, NM, and Livermore, CA, 2004).
5. T. Kim, S. Park, S. Jeong, Diffusion dynamics controlled colloidal synthesis of highly monodisperse InAs nanocrystals. *Nat. Commun.* **12**, 3013 (2021).
6. J. Jasieniak, M. Califano, S. E. Watkins, Size-dependent valence and conduction band-edge energies of semiconductor nanocrystals. *ACS Nano* **5**, 5888–5902 (2011).
7. S. Li, Y.-L. Cao, W.-H. Li, Z.-S. Bo, A brief review of hole transporting materials commonly used in perovskite solar cells. *Rare Metals* **40**, 2712–2729 (2021).
8. P. R. Brown *et al.*, Improved current extraction from ZnO/PbS quantum dot heterojunction photovoltaics using a MoO3 interfacial layer. *Nano Lett.* **11**, 2955–2961 (2011).
9. C.-H.M. Chuang, P. R. Brown, V. Bulović, M. G. Bawendi, Improved performance and stability in quantum dot solar cells through band alignment engineering. *Nat. Mater.* **13**, 796–801 (2014).
10. N. K. Elumalai *et al.*, Enhancing the stability of polymer solar cells by improving the conductivity of the nanostructured MoO 3 hole-transport layer. *Phys. Chem. Chem. Phys.* **15**, 6831–6841 (2013).
11. J. I. Michel, J. Dréon, M. Boccard, J. Bullock, B. Macco, Carrier-selective contacts using metal compounds for crystalline silicon solar cells. *Prog. Photovolt. Res. Appl.* **31**, 380–413 (2023).
12. J. Tang *et al.*, Quantum junction solar cells. *Nano Lett.* **12**, 4889–4894 (2012).
13. A. Stavrinadis, G. Konstantatos, Strategies for the controlled electronic doping of colloidal quantum dot solids. *Chemphyschem* **17**, 632–644 (2016).
14. H. Liu *et al.*, Systematic optimization of quantum junction colloidal quantum dot solar cells. *Appl. Phys. Lett.* **101**, 151112 (2012).
15. L. Asor *et al.*, Zn-doped P-type InAs nanocrystal quantum dots. *Adv. Mater.* **35**, e2208332 (2022).
16. L. Asor *et al.*, InAs nanocrystals with robust p-type doping. *Adv. Funct. Mater.* **31**, 2007456 (2021).
17. J. H. Song, H. Choi, H. T. Pham, S. Jeong, Energy level tuned indium arsenide colloidal quantum dot films for efficient photovoltaics. *Nat. Commun.* **9**, 4267 (2018).
18. Z. Zhang, J. T. Yates, Band bending in semiconductors: Chemical and physical consequences at surfaces and interfaces. *Chem. Rev.* **112**, 5520–5551 (2012).
19. H. Lu, G. M. Carroll, N. R. Neale, M. C. Beard, Infrared quantum dots: Progress, challenges, and opportunities. *ACS Nano* **13**, 939–953 (2019).
20. D. Knorr *et al.*, Bonding of cysteamine on InAs surfaces. *Appl. Surf. Sci.* **462**, 489–501 (2018).
21. D. V. Talapin, J.-S. Lee, M. V. Kovalenko, E. V. Shevchenko, Prospects of colloidal nanocrystals for electronic and optoelectronic applications. *Chem. Rev.* **110**, 389–458 (2010).
22. M.-J. Choi *et al.*, Ligand exchange at a covalent surface enables balanced stoichiometry in III–V colloidal quantum dots. *Nano Lett.* **21**, 6057–6063 (2021).
23. C. Giansante, Surface chemistry impact on the light absorption by colloidal quantum dots. *Chem. A Eur. J.* **27**, 14358–14368 (2021).
24. C. Giansante *et al.*, "Darker-than-black" PbS quantum dots: Enhancing optical absorption of colloidal semiconductor nanocrystals via short conjugated ligands. *J. Am. Chem. Soc.* **137**, 1875–1886 (2015).
25. H. Aqoma *et al.*, High-efficiency photovoltaic devices using trap-controlled quantum-dot ink prepared via phase-transfer exchange. *Adv. Mater.* **29**, 1605756 (2017).
26. W. Ahmad *et al.*, Lead selenide (PbSe) colloidal quantum dot solar cells with >10% efficiency. *Adv. Mater.* **31**, 1900593 (2019).
27. S. Kim *et al.*, One-step deposition of photovoltaic layers using iodide terminated PbS quantum dots. *J. Phys. Chem. Lett.* **5**, 4002–4007 (2014).
28. X. Zhang *et al.*, Inorganic CsPbI3 perovskite coating on PbS quantum dot for highly efficient and stable infrared light converting solar cells. *Adv. Energy Mater.* **8**, 1702049 (2018).
29. T.-G. Kim *et al.*, Trap passivation in indium-based quantum dots through surface fluorination: Mechanism and applications. *ACS Nano* **12**, 11529–11540 (2018).
30. A. Cros-Gagneux *et al.*, Surface chemistry of InP quantum dots: A comprehensive study. *J. Am. Chem. Soc.* **132**, 18147–18157 (2010).
31. Q. Zhao, H. J. Kulik, Electronic structure origins of surface-dependent growth in III–V quantum dots. *Chem. Mater.* **30**, 7154–7165 (2018).
32. J. Leemans *et al.*, Colloidal III–V quantum dot photodiodes for short-wave infrared photodetection. *Adv. Sci.* **9**, 2200844 (2022).
33. A. M. Najarian *et al.*, Sub-millimetre light detection and ranging using perovskites. *Nat. Electron.* **5**, 511–518 (2022).
34. J. Ilavsky, Nika: Software for two-dimensional data reduction. *J. Appl. Crystallogr.* **45**, 324–328 (2012).
35. J. Xu *et al.*, 2D matrix engineering for homogeneous quantum dot coupling in photovoltaic solids. *Nat. Nanotechnol.* **13**, 456–462 (2018).
36. G. Kresse, J. Furthmüller, Efficient iterative schemes for ab initio total-energy calculations using a plane-wave basis set. *Phys. Rev. B* **54**, 11169–11186 (1996).
37. J. P. Perdew, K. Burke, M. Ernzerhof, Generalized gradient approximation made simple. *Phys. Rev. Lett.* **77**, 3865–3868 (1996).
38. K. Lee, É. D. Murray, L. Kong, B. I. Lundqvist, D. C. Langreth, Higher-accuracy van der Waals density functional. *Phys. Rev. B* **82**, 081101 (2010).
39. A. Taguchi, K. Kanisawa, Stable reconstruction and adsorbates of InAs(111) A surface. *Appl. Surf. Sci.* **252**, 5263–5266 (2006).